Lattice expansion and local lattice distortion in Nb- and La-doped SrTiO_{3} single crystals investigated by x-ray diffraction and first-principles calculations

Shunsuke Kobayashi, Yuichi Ikuhara, and Teruyasu Mizoguchi

Phys. Rev. B **98**, 134114 — Published 31 October 2018

DOI: 10.1103/PhysRevB.98.134114

Lattice expansion and local lattice distortion in Nb- and La-doped $SrTiO_3$ single crystals investigated by X-ray diffraction and first-principles calculations

Shunsuke Kobayashi[1*], Yuichi Ikuhara[1,2] and Teruyasu Mizoguchi[3*]

[1]Nanostructures Research Laboratory, Japan Fine Ceramics Center, Atsuta, Nagoya 456-8587, Japan
[2]Institute of Engineering Innovation, The University of Tokyo, Bunkyo, Tokyo 113-8656, Japan
[3]Institute of Industrial Science, The University of Tokyo, Meguro, Tokyo 153-8505, Japan

*Corresponding author
E-mail: s_kobayashi@jfcc.or.jp (S. K.)
E-mail: teru@iis.u-tokyo.ac.jp (T. M.)

ABSTRACT

Electron-doped $SrTiO_3$ (where the dopant can be Nb or La) has been widely investigated for both its fundamental interest in condensed matter physics and for industrial applications. Its electronic properties are closely related to the Ti–O bonding states in the $SrTiO_3$ crystal. To further develop and control these properties, it is crucial to understand the factors controlling the change in lattice parameters and local lattice distortion upon doping with various atoms. Herein, we report the changes in lattice parameters and local lattice distortion in Nb- and La-doped $SrTiO_3$ single crystals, investigated by in-plane X-ray diffraction and first-principles calculations. The lattice parameter of Nb- and La-doped $SrTiO_3$ single crystals increased with dopant concentration. The broad intensities around the Bragg peak observed in the in-plane X-ray diffraction experiments indicated that the local lattice expansion and contraction, or local lattice distortions, in the crystal were caused by the dopant atoms. First-principles calculations similarly

showed that the lattice expansion and local lattice distortions in the $SrTiO_3$ crystals were caused by doped Nb and La atoms. Atoms surrounding Schottky pairs of O and Sr vacancies were displaced both away from and towards the vacancies, resulting in a reduction in the lattice expansion of donor-doped $SrTiO_3$. Donor atoms and Schottky pairs thus play an important role in determining the lattice parameters of $SrTiO_3$ crystals. These fundamental structural analyses provide a useful basis to further investigate the electronic conductivity of electron-doped $SrTiO_3$.

I. INTRODUCTION

Electron-doped strontium titanate ($SrTiO_3$) is an n-type oxide semiconductor that has been widely investigated in condensed matter physics owing to its high electron mobility [1-3], quantum phenomena [4,5], and superconductivity [6,7], as well as for its use in thermoelectric applications [8,9] and as an anode material in solid oxide fuel cells [10]. Stoichiometric $SrTiO_3$ is a typical ABO_3 perovskite oxide and an insulator. Electronic conductivity can be introduced by creating O vacancies through partial reduction [11], or by doping the A sites with rare earth (donor) atoms or the B sites with transition metal atoms. For example, electron-doped $SrTiO_3$ is typically obtained by partially substituting Nb for Ti and La for Sr. The lattice parameter of $SrTiO_3$ is known to increase with the concentration of the Nb [12,13] and La [14-16] dopants.

Changes in oxidation states upon substitution of aliovalent dopant atoms changes the effective ionic radii of the transition metals in the system. In Nb-doped $SrTiO_3$, Nb^{5+} replaces Ti^{4+}, and the resulting composition can be written as $Sr^{2+}Ti^{4+}_{1-2x}Ti^{3+}_{x}Nb^{5+}_{x}O^{2-}_{3}$ ($0 \leq x < 0.5$). Similarly, when La^{3+} ions substitute for Sr^{2+} in $SrTiO_3$, the resulting structure can be represented as $Sr^{2+}_{1-y}La^{3+}_{y}Ti^{4+}_{1-y}Ti^{3+}_{y}O^{2-}_{3}$ ($0 \leq y \leq 1$). In the case of Nb-doped $SrTiO_3$, lattice expansion can be

51 straightforwardly explained based on the increase in the total effective ionic radius when Ti^{4+}
52 (60.5 pm) is replaced with Nb^{5+} (64 pm), and some of the Ti^{4+} (60.5 pm) atoms are reduced to Ti^{3+}
53 (67 pm) [17]. In contrast, in La-doped $SrTiO_3$, although the effective ionic radius of the B cations
54 increases because of reduction of some Ti^{4+}, the effective ionic radius of the A cations decreases
55 upon replacing Sr^{2+} (144 pm) with La^{3+} (136 pm) [17]. The lattice expansion that occurs in the
56 case of La-doped $SrTiO_3$ crystals thus cannot be explained simply as a change in effective ionic
57 radii upon doping.

58 Janotti et al. revealed that changes in the electronic states of some atoms is an important factor
59 in the lattice expansion of La-doped $SrTiO_3$ [14]. On the other hand, it has also been reported that
60 the lattice parameter of La-doped $SrTiO_3$ decreases with an increase in dopant concentration,
61 which was attributed to the formation of non-ionized O vacancies [18,19]. As perovskite oxides
62 contain several different types of point defects, it is possible that formation of complex defects
63 [12,20-24] and their interactions with dopant atoms are responsible for the observed changes in
64 lattice parameters.

65 Dopant atoms in the crystal are also expected to alter not only the overall lattice parameter but
66 also the local crystal lattice surrounding the dopant atoms [25]. Changes in interatomic spacings
67 and local lattice distortions as a result of changes in the ionic radii and electronic states upon
68 introduction of donor atoms in $SrTiO_3$ are ultimately related to changes in Ti–O bonding states,
69 which determine the material's band structure [26-31]. Changes in Ti–O bonding states, and
70 distortions in the $SrTiO_3$ crystal structure, are known to decrease the effective mass of electrons,
71 because of changes in the shape and degeneracy of the conduction band [28-30]. In particular, the
72 electron mobility in the crystal at room temperature is known to be influenced by longitudinal
73 optical (LO) phonon scattering [32]. Lattice distortions can also lower the LO phonon frequency,

reduce scattering, and possibly improve the overall conductivity [31]. Elucidating the mechanism of the lattice changes upon doping Nb and La atoms into the $SrTiO_3$ crystal is thus an important step in understanding the electronic properties of the doped material.

Herein, we report the lattice expansion and local lattice distortions in Nb- and La-doped $SrTiO_3$ single crystals investigated both experimentally and theoretically. Lattice parameters of Nb- and La-doped $SrTiO_3$ single crystals increased with the dopant concentration. During in-plane X-ray diffraction (XRD) analysis, broad intensities around the Bragg peak for the Nb- and La-doped $SrTiO_3$ single crystals were observed, indicating that both lattice expansion and contraction, i.e., local lattice distortions, occurred in the crystals as a result of doping. This finding was confirmed by first-principles calculations. Furthermore, Schottky-like pairs of O and Sr vacancies were found to be capable of reducing the lattice expansion in both systems, because some atoms in the vicinity of the vacancies were displaced away from them and others toward them. These results provide useful insights into the influence of local structural changes on the electronic conductivity of electron-doped $SrTiO_3$.

II. METHODOLOGY

A. Experimental procedure

Commercially available Nb-, La- and non-doped $SrTiO_3$ single crystals (Furuuchi Co.), which were grown by the Verneuil method, were used in this study. The surfaces of all the crystals were treated by chemical-mechanical polishing. The Nb concentrations in $SrTi_{1-x}Nb_xO_3$ were 0.02 (x = 0.0002), 0.1 (x = 0.001), 0.2 (x = 0.002), 1.0 (x = 0.01), and 2.0 at.% (x = 0.02). The La

concentrations in $Sr_{1-y}La_yTiO_3$ were 0.1 (y = 0.001), 0.5 (y = 0.005), 1.0 (y = 0.01), and 5.0 at.% (y = 0.05). The size of the samples was about 5 × 5 × 0.5 mm^3.

Out-of-plane and in-plane XRD measurements were performed using a laboratory XRD system (SuperLab, Rigaku Co. [33]) at room temperature (24 °C). An incident X-ray source with a combined microfocus X-ray generator and multilayer confocal mirror optics was used, operated at 40 kV and 30 mA with Cu $K\alpha_1$ (λ = 0.154059 nm) radiation. A monochromator and a diffracted-beam analyzer, both two-bounce Ge (220) channel-cut crystals, were used. The widths of the vertical and horizontal divergence slits were set to 1.2 and 1.8 mm, respectively. The widths of the vertical and horizontal receiving slits were set to 2 and 4 mm, respectively. These slit widths were set to the substantial maximum values of the incident X-ray source width and the acceptance angle of the diffracted-beam analyzer crystal. A schematic drawing of the experimental setup used for the in-plane XRD measurements is shown in Fig. S1.

The irradiation width in the vertical direction along the incident X-ray is approximately 1.8 mm, depending on the horizontal divergence slit, and that in the parallel direction is approximately 20 to 30 mm, depending on the incidence angle. The incidence angles for the in-plane measurements were set to approximately 0.35° to 0.40°, slightly larger than the critical angle α_c (~0.31°) of $SrTiO_3$. For these incidence angles, the X-ray attenuation length or penetration depth was approximately 80 nm [34-36]. Under these optical conditions, the full width at half maximum (FWHM) of the rocking curve of the 020 reflection in the non-doped $SrTiO_3$ single crystal was 0.0030° (10.8 arcsec), in good agreement with that from a study on $SrTiO_3$ single crystals [37].

B. Calculation procedure

The lattice expansion and local lattice distortions of Nb- and La-doped $SrTiO_3$ were investigated using first-principles calculations within the framework of the projector augmented wave (PAW) method based on density functional theory (DFT). To determine the donor-doped electronic structure correctly, spin-polarized calculations were performed. The exchange-correlation potential was treated using the generalized gradient approximation (GGA), and the on-site Coulomb potential was set at the Ti 3d orbital with U = 4.36 eV [38], Nb 4d orbital with U = 5.00 eV [39], and La 4f orbital with U = 10.32 eV [40], as implemented in the VASP code [41,42]. The cutoff energy for the planewave basis sets was 500 eV. Supercells containing 40, 135, 320, 625, and 1,080 atoms were generated by repeating the unit cell of $SrTiO_3$ 2 × 2 × 2, 3 × 3 × 3, 4 × 4 × 4, 5 × 5 × 5, and 6 × 6 × 6 times, respectively, along each of the principal directions. The k-point sampling in the Brillouin zone was performed using 4 × 4 × 4 (40 atoms), 3 × 3 × 3 (135 atoms), and 2 × 2 × 2 (320 atoms) meshes, including the Γ point, using a Monkhorst–Pack scheme, and single Γ-point calculations were performed for the 625-atom and 1,080-atom supercells. Each supercell contained either one dopant atom, one vacancy, one or two electronic defects, a single dopant/vacancy pair, or a combination of these in the case of cluster calculations. The dopant and vacancy concentrations of the 40-, 135-, 320-, 625-, and 1,080-atom supercells were approximately 12.5, 3.7, 1.6, 0.8, and 0.46 at.%, respectively. The lattice and atomic positions were fully optimized until the residual forces on all the atoms were below 0.03 eV/Å. In the calculations of charged vacancies, the total charge of the supercells was neutralized using a jellium background charge.

For dopant concentrations below 5 at.%, Nb- and La-doped $SrTiO_3$ were cubic at room temperature, without TiO_6 octahedra rotations [15,43]. To minimize the effect of octahedral rotation, simulations were performed under symmetry constraints; in most cases (i.e., single defect models), O_h symmetry was applied.

It is known that the Pulay stress is an important factor affecting cell-size relaxation. The estimated Pulay stresses in the primitive cell calculations using cut-off energies of 400, 500, and 600 eV were 1.29, -0.26, and 0.14 × 10^3 bar, respectively, indicating that the 400 eV calculation provides inaccurate results. In this study, to perform systematic calculations for large models containing more than 1,000 atoms, we selected 500 eV as the cut-off energy despite its lower accuracy compared with 600 eV. For low concentrations (320-, 625-, and 1,080-atom supercells) of Nb-doped $SrTiO_3$, the calculated Pulay stresses were 0.2–0.4 × 10^3 bar, which are not greatly different from those in other calculations. Based on these preliminary results, we adjudged the present conditions to be sufficiently accurate for performing cell-size relaxation.

III. RESULTS AND DISCUSSION

A. Out-of-plane and in-plane XRD patterns of non-doped $SrTiO_3$ single crystal

Figure 1a shows the out-of-plane and in-plane XRD patterns obtained from a non-doped $SrTiO_3$ single crystal. The out-of-plane and in-plane XRD patterns were measured under the same optical conditions, using 002 and 020 reflections of $SrTiO_3$, respectively. The FWHM of the peaks of the out-of-plane and in-plane XRD patterns are 0.0066° and 0.0052°, respectively, indicating that both XRD patterns have a similar FWHM value. In contrast, the full width at tenth maximum (FWTM) of the out-of-plane and in-plane peaks are 0.0128° and 0.0092°, respectively, indicating that the peak shape of the out-of-plane pattern becomes much wider than that of the in-plane pattern with an increase in the distance from the Bragg peak. This is because of the effect of crystal truncation rod (CTR) scattering, which originates from the interface between the crystal surface and vacuum in the out-of-plane XRD pattern [44,45]. Conversely, when measuring in-plane diffraction, the intensity can be regarded as corresponding to diffraction from an

165 infinitely continuous crystal without any interface between the crystal surface and vacuum.
166 Hence, the in-plane pattern can be obtained directly from the intensity of the diffracted X-rays,
167 without taking the intensity of the CTR scattering into account.

168 The influence of CTR scattering on the out-of-plane XRD pattern can be more clearly observed
169 on a log-scale intensity axis, as shown in Fig. 1b. For the out-of-plane method, the small peak
170 intensities caused by the dopant atoms in the crystal are buried under the intensity of the CTR
171 scattering. To detect the slight lattice distortions originating from dopant atoms in the crystal,
172 in-plane analysis is a more powerful method because the peak shape of the in-plane XRD pattern
173 is sharp in the absence of CTR scattering, as shown in the inset of Fig. 1b. In this study, we
174 therefore investigated the lattice parameter and local lattice distortions using the in-plane XRD
175 technique.

176

177 **B. Lattice expansion in Nb- and La-doped $SrTiO_3$ single crystals**

178 Figure 2 compares the in-plane XRD patterns obtained from the non-, Nb-, and La-doped
179 $SrTiO_3$ single crystals. Each Bragg peak shifted to a lower angle, indicating that the overall lattice
180 parameter increased with dopant concentration, as shown in Figs. 2b and 2d. The relationships
181 between lattice expansion and concentration of the two dopants is in good agreement with earlier
182 powder diffraction results [12-16].

183 Figure 3 shows the lattice parameters of Nb- and La-doped $SrTiO_3$ as a function of dopant
184 concentration. The lattice parameter of the non-doped $SrTiO_3$ single crystal was a = 0.39051(9)
185 nm; the structure was estimated from the 020 diffraction to be that of a cubic perovskite, in good
186 agreement with an earlier study of $SrTiO_3$ single crystals (a = 0.3905268 nm) [37]. In the case of
187 Nb- and La-doped $SrTiO_3$, lattice parameters increased with dopant concentration. Results of

lattice parameter and rocking curve measurements for the Nb- and La-doped $SrTiO_3$ single crystals are summarized in Table 1, with plots of the rocking curves provided in Supplemental Material as Fig. S6.

Defect formation in complex perovskite oxides is closely related to lattice expansion [12,20-24]. In this study, the non-, Nb-, and La-doped $SrTiO_3$ single crystals were grown by the Verneuil method [46]. In this method, the atmosphere for crystal growth is reducing because of the presence of hydrogen gas and because the flame temperature for melting the starting materials is approximately 2,000°C. Under a reducing atmosphere and at high growth temperatures, the Ti vacancies can be ignored because of the high formation energy for the $SrTiO_3$ crystal [47]. The mass-action relationship between Sr and O vacancies is $[V_{Sr}''][V_O^{\bullet\bullet}] = Ks(T)$, where $Ks(T)$ is the temperature-dependent formation constant [48], and the substitution and defect states are described using Kröger–Vink notation [49]. The mass-action relationship indicates that the concentration of V_{Sr}'' can be decreased by increasing the concentration of $V_O^{\bullet\bullet}$ at high temperatures and under a reducing atmosphere [48,50]. For donor (D)–doped $SrTiO_3$, the mass-action relationship between O vacancies and donors in the as-grown $SrTiO_3$ crystal under a reducing atmosphere becomes $[V_O^{\bullet\bullet}] > [D^{\bullet}] > [V_{Sr}'']$ [12,48,50]. After annealing treatments to remove only the O vacancies from donor-doped $SrTiO_3$ crystals [46,51], the mass-action relationship can be assumed to be $[D^{\bullet}] > [V_O^{\bullet\bullet}] \approx [V_{Sr}'']$. This leads to the favorable situation of having only residual O vacancies, owing to the lower energy of formation of the $V_O^{\bullet\bullet} + V_{Sr}''$ partial Schottky defect compared with that of a single Sr vacancy [47]. These considerations suggest that doping of $SrTiO_3$ single crystals should influence the lattice expansion by altering the balance between different defect concentrations, even though both Sr and O vacancies will still be present in the crystal to a certain degree.

In $SrTiO_3$ crystals grown by the Verneuil process, several other types of defect are known to be

present in addition to point defects and donor atoms [52-54]. It is possible that such extended defects and inhomogeneities may also affect the Bragg peak in in-plane XRD measurements. In this study, using XRD topography, transmitted light microscopy, low- and high-magnification scanning transmission electron microscopy, as well as analyzing the measurement location dependence using in-plane XRD, we detected a number of extended defects, primarily misorientations and domain boundaries; details are given in Section 3 of Supplemental Material. Although use of samples of higher crystallinity (fewer extended defects) is to be preferred, the concentrations of the extended defects were deemed to be sufficiently low that the experimentally observed structures and properties of our Nb- and La-doped $SrTiO_3$ single crystals could be interpreted primarily in terms of local lattice expansion and distortion around dopants.

C. Local lattice distortions in Nb- and La-doped $SrTiO_3$ single crystals

Broad intensities around the Bragg peak, indicated by the red and black arrows in Figs. 2a and 2c, were observed for Nb- and La-doped $SrTiO_3$ single crystals. These broad peaks indicate that there are regions of local lattice expansion (black arrows) and contraction (red arrows) within the crystal. In neither case could the broad peaks be fitted with a single Gaussian curve. For example, Fig. 4 shows the region around the Bragg peak in the case of 0.02 at.% Nb-doped $SrTiO_3$. The magnitudes of local lattice expansion and contraction ranged from 0.05 to 0.19 pm and from 0.04 to 0.22 pm (Table 2), respectively, as calculated by the difference between the peak centers of the Gaussian curves and the Bragg peak. This suggests that there are different regions in the crystal with different magnitudes and extents of local lattice distortion, whether in compression or tension.

Gaussian curves corresponding to expanded and contracted regions are shown as dotted orange and blue lines in Fig. 4a, respectively, and the ratios of the summed intensities of the two sets are

236 plotted in Figs. 4b and 4c as a function of dopant concentration. The fitted curves for all the
237 in-plane XRD patterns are shown in Fig. S2 of Supplemental Material.

238 For both Nb- and La-doped $SrTiO_3$, contraction and expansion intensities are larger and more
239 diverse than those of non-doped $SrTiO_3$. Contraction intensities of the Nb- and La-doped $SrTiO_3$
240 crystals generally decrease with increasing dopant concentration, except in the case of 5 at.%
241 La-doped $SrTiO_3$, where the intensity increases markedly compared to the 1 at.% crystal. On the
242 other hand, the expansion intensities do not depend strongly on the dopant concentration, and the
243 contraction intensities are larger than the expansion intensities for both Nb- and La-doped
244 $SrTiO_3$.

245 Figure 4d shows the ratios of the contraction intensities of the Nb- and La-doped $SrTiO_3$ single
246 crystals as a function of the FWHM of the rocking curves. The contraction intensities of the two
247 crystals tend to increase with the FWHMs of the rocking curves. This indicates that the peak
248 widths of the in-plane XRD patterns and rocking curves broaden with a decrease in dopant
249 concentration. The FWHMs of the rocking curves provide information on the crystallinity or lack
250 thereof, e.g., misorientations [53,55], dislocation densities [56,57], and other defects. In this study,
251 we carefully examined the misorientations, dislocations, and inhomogeneities in $SrTiO_3$ single
252 crystals, and details of these measurements with further discussion are provided in Section 3 of
253 Supplemental Material. The broad intensities around the Bragg peak and the FWHMs of the
254 rocking curves were found to be only weakly influenced by these extended defects, however.

255 The above analysis indicates that the overall lattice expansion and local lattice distortions in Nb-
256 and La-doped $SrTiO_3$ single crystals depend on the nature and concentration of the dominant
257 defects, including dopant atoms.

258

259 **D. Calculations of dopant atoms and point defects in $SrTiO_3$ crystals.**

To understand the influence of various kinds of defects on lattice expansion and local lattice distortions in doped $SrTiO_3$, further first-principles calculations were performed using supercells of different sizes containing positively charged defects $Nb_{Ti}^{\bullet}$, $La_{Sr}^{\bullet}$, and $V_O^{\bullet\bullet}$; neutral defects Nb_{Ti}^{x}, La_{Sr}^{x}, and V_O^{x}; or isolated charges e' and $2e'$. In standard Kröger–Vink notation, Nb_{Ti}^{x}, La_{Sr}^{x}, and V_O^{x} imply that the electrons are localized on the defect, but it is more likely that the electron is donated to the transition metal atoms, so to represent this situation we write these defects as $Nb_{Ti}^{\bullet} + e'$, $La_{Sr}^{\bullet} + e'$, and $V_O^{\bullet\bullet} + 2e'$ from here on. This was confirmed by the unbonded electrons becoming delocalized within the conduction bands (CB) of the neutral defect and isolated electron systems.

Figure 5 shows schematic band structures of each electron- or donor-doped system. No extra electrons are available to enter the CB in the case of states i, ii, and iii, i.e., perfect (undoped) $SrTiO_3$ and positively charged dopant or defect systems. Relaxation of the crystal structure around these defects reveals the effects of positively charged point defects (both extrinsic and intrinsic) on the lattice parameter, absent the effects of electrons in the CB or the creation of subvalent Ti ions. In the case of systems containing net neutral defect states, viz., $Nb_{Ti}^{\bullet} + e'$, $La_{Sr}^{\bullet} + e'$, and $V_O^{\bullet\bullet} + 2e'$, the electrons are located in the CB, as is also the case for the electron-doped systems. Examining the relaxed structures of these systems sheds further light on the effect of dopant atoms and point defects (including trivalent Ti ions) under the appropriate experimental conditions.

E. Lattice parameter changes resulting from positively charged defect states

Changes in lattice parameter, ΔL, were calculated according to $\Delta L = L_a - L_{STO}$, where L_{STO} is the calculated lattice parameter of non-doped $SrTiO_3$ (0.397694 nm) and L_a is the calculated lattice parameter from supercells of $SrTiO_3$ containing dopant and/or other defect species. Figure

6 shows a plot of calculated changes in lattice parameter for models containing positively charged defects ($Nb_{Ti}^{\bullet}$, $La_{Sr}^{\bullet}$, and $V_O^{\bullet\bullet}$), as a function of dopant concentration. As summarized in the illustrations in Fig. 5, no extra electrons were present in the CBs for these defect species.

In the case of the $La_{Sr}^{\bullet}$ containing system, the lattice parameter decreased because of a decrease in the effective ionic size of the A-site cations when Sr^{2+} is replaced with La^{3+}. In the case of $Nb_{Ti}^{\bullet}$, however, the lattice parameter changed only slightly, owing to the smaller difference in ionic radii between Nb^{5+} and Ti^{4+}. For the double-charged O vacancy, $V_O^{\bullet\bullet}$, the lattice parameter decreased with increasing vacancy concentration, consistent with the removal of the large O^{2-} ions.

Previous calculations have shown that when vacancies are present in ionic crystals such as perovskite oxides the local lattice around the vacancy often expands as a result of the electrostatic repulsion between its neighboring cations [22]. Our calculations of $V_O^{\bullet\bullet}$-containing $SrTiO_3$ suggest that contraction of the lattice beyond the neighboring cation shell is enough to compensate for this expansion, producing an overall decrease in lattice volume. This suggests that the lattice contraction reported previously for La-doped $SrTiO_3$ may have been caused by anion vacancies (i.e., oxygen substoichiometry) in the crystals [18,19].

F. Lattice parameter changes for neutral defect systems

In contrast to the above defect species, the neutral defect systems $Nb_{Ti}^{\bullet} + e'$, $La_{Sr}^{\bullet} + e'$, and $V_O^{\bullet\bullet} + 2e'$, and free electron states e' and $2e'$, produced local lattice expansion with increasing dopant concentration, as seen in Fig. 7. Because positively charged defects on their own result in lattice contraction (Fig. 6), the presence of electrons in the CB, corresponding to creation of trivalent Ti species, appears to be responsible for the overall lattice expansion in these cases. This is most noticeable in systems containing free charges, as the increase in lattice parameters is greatest (Fig.

7).

The $SrTiO_3$ crystal with $V_O^{\bullet\bullet} + 2e'$ exhibits only a small lattice expansion even when the dopant concentration is above 12 at.%. This is because the decrease in lattice volume caused by the positively charged vacancy is counterbalanced by the increase due to the larger ionic size of trivalent Ti ions. The slight change in lattice parameter for $V_O^{\bullet\bullet} + 2e'$ predicted from our calculations is consistent with the earlier experimental results obtained for O-deficient $SrTiO_3$ [11,58]. In contrast, lattices of systems containing $Nb_{Ti}^{\bullet}$ and $La_{Sr}^{\bullet}$ expanded when donor electrons were also included.

To examine the origin of the lattice expansion caused by $Nb_{Ti}^{\bullet} + e'$ and $La_{Sr}^{\bullet} + e'$ dopant states in more detail, we compared the calculated lattice parameters with experimental values of Nb- and La-doped $SrTiO_3$ crystals as a function dopant concentration, as shown in Fig. 8a. Both experiment and theoretical modeling indicate that the rates of expansion for La-doped $SrTiO_3$ are smaller than those for the Nb-doped $SrTiO_3$ crystals, suggesting that the theoretical models describe an important mechanism behind the lattice expansion. However, although the experimental trend is qualitatively reproduced by the DFT calculations, the absolute values of the lattice parameters are overestimated for both dopants (Fig. 8a).

One of the reasons for the discrepancy between the calculated and experimental values could be that in the real materials defect complexes (clusters) form with native defects, such as partial Schottky defects $V_O^{\bullet\bullet} + V_{Sr}''$. To examine the effect of such defect complexes on the crystal lattice, we performed DFT calculations of models containing various combinations of defects with V_{Sr}'' and/or $V_O^{\bullet\bullet}$, and the results are summarized in Fig. 8b. Lattice parameters of crystals containing point defects $V_{Ti}'' + 4h^{\bullet}$, $V_{Sr}'' + 2h^{\bullet}$, $V_O^{\bullet\bullet} + 2e'$, $2Nb_{Ti}^{\bullet} + V_{Sr}''$, and $2La_{Sr}^{\bullet} + V_{Sr}''$, as well as the Schottky pair $V_{Sr}'' + V_O^{\bullet\bullet}$, all increased as a result of electrostatic repulsion between the host cations surrounding the point defects [22]. The magnitude of the lattice expansion in the case

of the $V_O^{\bullet\bullet}$ + V_{Sr}'' cluster (half-filled diamond symbol in Fig. 8b) is smaller than the sum of the lattice expansions produced by $V_O^{\bullet\bullet}$ + 2e′ (filled triangle symbol in Fig. 8b) and V_{Sr}'' + $2h^{\bullet}$ (reversed triangle symbol in Fig. 8b) defect states in isolation, indicating that interaction between point defects and absence of free electrons abates much of the inter-ion repulsion, leading to reduced overall lattice expansion.

Figure 8b shows that lattice expansion around dopant atoms is decreased in the vicinity of $V_O^{\bullet\bullet}$ + V_{Sr}'' Schottky-type pairs. As partial Schottky defects in $SrTiO_3$ are more energetically favorable than full Schottky defects [47], this may explain the large difference between the magnitudes of lattice expansion observed experimentally and those predicted from DFT using isolated dopant atoms and electrons only. In contrast to partial Schottky defects, defect clusters of the form $2Nb_{Ti}^{\bullet}$+ V_{Sr}'' and $2La_{Sr}^{\bullet}$+ V_{Sr}'' cannot explain the difference between the experimental and simulation results, as both produce an excessive lattice expansion, despite $La_{Sr}^{\bullet}$ dopants on their own being shown to cause lattice contraction (Fig. 6). These results suggest that charged O vacancies $V_O^{\bullet\bullet}$ are important in abating lattice expansion of donor-doped $SrTiO_3$.

To better understand the relaxation behavior around vacancy pairs and dopants, we plotted local cation displacements in the vicinity of dopants/defects as vector images. Figure 9 shows the three-dimensional vector plots of Sr ion displacements around $Nb_{Ti}^{\bullet}$ + e′, $Nb_{Ti}^{\bullet}$ + e′ + $V_O^{\bullet\bullet}$ + V_{Sr}'', $La_{Sr}^{\bullet}$ + e′, and $La_{Sr}^{\bullet}$ + e′ + $V_O^{\bullet\bullet}$ + V_{Sr}'' defect clusters in the 625-atom supercell, corresponding to the results in Fig. 8b. The vectors indicate the magnitudes and directions of the displacements from the ideal cubic perovskite lattice positions, estimated using the calculated supercell volume. Since the displacements of the Ti and O ions were much smaller than those of the Sr ions, for clarity only the displacements of the Sr ions are shown. The Sr ions adjacent to $Nb_{Ti}^{\bullet}$ + e′ (Fig. 9a) and $La_{Sr}^{\bullet}$ + e′ defects (Fig. 9b) are uniformly displaced away from the defects (expansion). The maximum displacements of the Sr ions near $Nb_{Ti}^{\bullet}$ + e′ and $La_{Sr}^{\bullet}$ + e′ defects are 3.6 and 1.5

pm, respectively. The difference in the magnitude of these displacements depends on the type of dopant, indicating that this plays a decisive role in determining the total lattice expansion.

For each donor/Schottky pair cluster, the Sr ion displacements are larger than those for the single dopant atoms (maximum ~5.0 pm for $Nb_{Ti}^{\bullet} + e' + V_O^{\bullet\bullet} + V_{Sr}''$ and ~3.9 pm for $La_{Sr}^{\bullet} + e' + V_O^{\bullet\bullet} + V_{Sr}''$), as shown in Figs. 9c and 9d. In addition, the directions of displacement vectors of Sr ions around the Schottky pair are not uniform, and some relax towards the defect (local contraction). This complex arrangement of cation displacements caused by the Schottky pair reduce the strain field induced by the dopants or other point defects in the crystal, resulting in a reduction in the overall lattice expansion of donor-doped $SrTiO_3$.

When the Sr and O vacancies of the Schottky pair are far away from each other in the supercell, the lattice parameter, L_a (~0.397851 nm for $Nb_{Ti}^{\bullet} + e' + V_O^{\bullet\bullet} + V_{Sr}''$, or ΔL = ~0.157 pm, and ~0.397762 nm for $La_{Sr}^{\bullet} + e' + V_O^{\bullet\bullet} + V_{Sr}''$, or ΔL = ~0.068 pm), is slightly larger than when the Sr and O vacancies are close together, such as in the model shown in Fig. 9c (L_a = ~0.397829 nm or ΔL = ~0.135 pm) and Fig. 9d (L_a = ~0.397759 nm or ΔL = ~0.065 pm), respectively, although in both cases the partial Schottky pair has an ameliorating effect on lattice expansion. This indicates that it is necessary to take into account both the arrangement and concentration of the dopants and point defects in the crystal to obtain a more accurate model using this theoretical approach. This may be challenging because the first-principles calculations are already computationally intensive owing to the size of the supercell and relatively large atom displacements during lattice relaxation. Nevertheless, the present results provide useful insights into the local changes in bonding environments and lattice strains caused by electron doping of $SrTiO_3$.

G. Local lattice distortion induced by dopant atoms

To further understand the changes caused by the dopants and vacancies, we analyzed the local

380 lattice expansion and contraction around the dopants in the calculated models in terms of
381 individual lattice cells. This was done by calculating the distances between A-site cations in
382 individual cells (i.e., cell lengths)) as well as B-site cations in individual cells for each relaxed
383 supercells. It is important to consider both the A-centered cells and B-centered cells because
384 changes in both sublattices influence the shape of the reciprocal lattice and hence Bragg peak.

385 As an example, Figures 10a and 10b show the relaxed structures of the 6 × 6 × 6 (1,080 atoms;
386 dopant concentration approximately 0.46 at.%) supercells for $Nb_{Ti}^{\bullet} + e'$ and $La_{Sr}^{\bullet} + e'$ systems,
387 respectively, sliced through the plane of the dopant atom with background colors indicating the
388 magnitude of the area ratio $S_{Sr\text{-}site}/S_{ave}$, where $S_{Sr\text{-}site}$ is the projected area bounded by Sr sites at
389 the corners of a single cell, and S_{ave} is the projected area of the ideal cubic perovskite unit cell for
390 the relaxed supercell.

391 In both doped systems, the Sr and Ti atoms immediately adjacent to the dopant atoms are
392 displaced away from the dopants. The magnitudes of the displacements are greater in the case of
393 the $Nb_{Ti}^{\bullet} + e'$ system than the $La_{Sr}^{\bullet} + e'$ system, but in both cases Sr atoms are displaced slightly
394 more than Ti atoms. Compared to the nearest-neighbor cations, O ions adjacent to Nb are only
395 slightly displaced from their ideal sites, away from the Nb atom as a result of the larger ionic
396 radius of Nb^{5+} compared to Ti^{4+}. In contrast, nearest-neighbor O ions around La undergo a much
397 larger displacement towards the dopant because the relative increase in effective charge is larger
398 and is concentrated in a smaller volume, La^{3+} having a smaller ion radius than Sr^{2+}.

399 The differences in the responses of the cations can be explained in terms of the different
400 coordination environments of the A- and B-site cations and the response of the nearest-neighbor
401 O atoms to the introduction of a donor dopant; contraction of the O shell (12 atoms) around La on
402 the Sr site effectively shields the nearest shell of Ti ions from the increase in positive charge,
403 whereas the movement away from the Nb on the Ti site of the O shell (6 atoms) exposes the

nearest shells of Sr and Ti cations to the increased effective charge of the dopant, resulting in greater repulsion and hence expansion of the cells adjacent to the dopant-containing cell. In the case of 0.46 at.% $Nb_{Ti}^{\bullet} + e'$ model, expansion of the cells continues to the boundary of the supercell in the three principal axis directions. In the case of B-site doping, expansion is confined to the cells surrounding the dopant atom.

The displacements of Ti and Sr cations, and hence magnitudes of the cell contraction, decrease with increasing distance from the dopant, with cations at the midplane between two supercells remaining on ideal perovskite sites because of the balancing forces from dopants in image supercells. Within a single supercell, the net effect of the cation repulsion and anion attraction in the nearest-neighbor shells is a local lattice expansion ($S_{Sr\text{-}site}/S_{ave} > 1$) which subjects the outer shells of cations to compressive strain fields ($S_{Sr\text{-}site}/S_{ave} < 1$), as seen in Figs. 10a and 10b.

Plots of the ratio $S_{Sr\text{-}site}/S_{ave}$ as a function of position in the lattice allow the distribution of expanded and contracted regions, and their relative magnitudes, to be analyzed. Figure 11 shows results for the 0.46 at.% $Nb_{Ti}^{\bullet} + e'$ system. Results for the $La_{Sr}^{\bullet} + e'$ system are included in Fig. S10 of Supplemental Material. Figure 11a is a histogram of cell lengths (for clarity, only a narrow range either side of the average (overall) lattice parameter is shown), which reveals that more lattice cells are compressed than expanded. Expanded cells are primarily those adjacent to the dopant, as seen in Fig. 10 and the inset of Fig. S10a, whereas compressed cells are dispersed over a wider volume and further from the dopant. As the large local expansion near the dopant is repeated periodically in image supercells, the compressed regions are mirrored across the periodic boundaries between supercells. Although lattice expansion adjacent to the dopant is to a large extent cancelled by compression of outer regions, the overall effect is a slight expansion of the lattice, corresponding to an increase in the lattice parameter of the supercell, L_a. For the 0.46 at.% $Nb_{Ti}^{\bullet} + e'$ system, the average Sr-centered and Ti-centered cell lengths were both 0.39792

428 nm, very close to that of the supercell as a whole (L_a = ~0.39790 nm), and greater than that of the
429 undoped system, L = 0.39051 nm.

430 Figures 11b and 11c show plots of the ratios of compressed and expanded cells, respectively, as
431 a function of dopant concentration. Because the experimental lattice parameters in Table 2 vary
432 by approximately ±0.25 pm, only contracted cells falling in the range $-0.25 < \Delta L < 0$ and
433 expanded cells within $0 < \Delta L < 0.25$ were used when calculating these ratios. The plots show that
434 the number of contracted cells of Nb- and La-doped $SrTiO_3$ decrease with increasing dopant
435 concentration, except in the case of 3.7 at.% La-doped $SrTiO_3$. In contrast, the number of
436 expanded cells does not appear to depend on the dopant concentration to any meaningful degree.
437 Furthermore, the number of contracted cells is higher than the number of expanded cells in both
438 cases; in other words, the increase in crystal lattice volume is concentrated in the region
439 immediately surrounding the dopant. Although the highest dopant concentration in the theoretical
440 models was only 0.46 at.%, the pattern or distribution of contracted and expanded regions is
441 consistent with the experimental results in Fig. 4.

442 The computational results also indicate that local lattice distortions depend strongly on the
443 dopant concentrations. The average distance between dopant atoms increases with decreasing
444 dopant concentration in the manner shown in Fig. 12. In the region of low dopant concentrations,
445 e.g., below 0.1 at.%, regions of lattice contraction are caused by local lattice expansion
446 immediately surrounding the dopant atoms, as illustrated in the schematic model in Fig. 12. For
447 lower dopant concentrations, e.g., below 0.001 at.%, the volume of unstrained crystal (regions far
448 from dopants) is much larger than that of regions of lattice contraction and expansion, so the
449 overall lattice parameter varies only slightly from that of the undoped crystal. For dopant
450 concentrations greater than 1 at.%, dopant atoms are sufficiently close to each other (~2 nm or 5
451 unit cells) that the regions between them undergo expansion only. In these two cases (low and

high dopant concentrations), the strain field distributions are more or less uniform, with less variation in local lattice distortions than is observed for intermediate dopant contents (0.1 to 1.0 at.%).

The above computational results are consistent with the in-plane XRD measurements, which indicated that, as a volume percent, more of the lattice is in compression than tension in donor-doped crystals (Fig. 2). Although smaller in volume, the magnitude of lattice expansion in tensile regions is greater than the net contraction further away from the dopants, resulting in an overall increase in lattice parameter, as predicted from theoretical calculations. It is thus reasonable to conclude that one of the chief contributors to broadening of the Bragg peak, corresponding to expanded and contracted regions of the lattice, are the donor atoms themselves.

IV. CONCLUSIONS

Lattice parameters and local lattice distortions of Nb- and La-doped $SrTiO_3$ single crystals were investigated through XRD measurements and first-principles calculations. The lattice parameters of Nb- and La-doped $SrTiO_3$ were found to increase with dopant concentration. In-plane XRD measurements allowed for detailed investigation of the sharp Bragg peak without any interference from CTR scattering. The broad intensities around the Bragg peak in Nb- and La-doped $SrTiO_3$ single crystals indicated the existence of local lattice distortions in the crystal. DFT calculations showed that the lattice expansions and local lattice distortions of Nb- and La-doped $SrTiO_3$ can be attributed to the introduction of donor dopant atoms. Lattice expansion was predominantly driven by the creation of trivalent Ti ions with electrons in the CB. The cationic displacements around the donor atoms resulted in the expansion of the local lattice, with locally contracted regions further from the defect. Formation of $V_{Sr}'' + V_O^{\bullet\bullet}$ partial Schottky defects reduced the lattice expansion of Nb- and La-doped $SrTiO_3$ because some of the atoms

476 surrounding the vacancies and dopant atoms displace away from these point defects whereas
477 other displace towards them. These results provide a consistent explanation of the influence of
478 dopants on the electronic conductivity of electron-doped $SrTiO_3$ in terms of local structural
479 distortions.
480

481 **ACKNOWLEDGEMENTS**

482 The authors thank C. A. J. Fisher and T. Yamamoto for the useful discussions. This work was
483 supported by a Grant-in-Aid for Young Scientists B (Grant No. 17K14119), Scientific Research
484 grants (Grant Nos. 25106003, 26249092, 17H06094) from the Japan Society for the Promotion of
485 Science, JST-PRESTO, and Kazato Research Foundation of Japan. Part of this work was
486 supported by the "Nanotechnology Platform" (project No. 12024046) sponsored by the Ministry
487 of Education, Culture, Sports, Science and Technology of Japan.

488 **Captions**

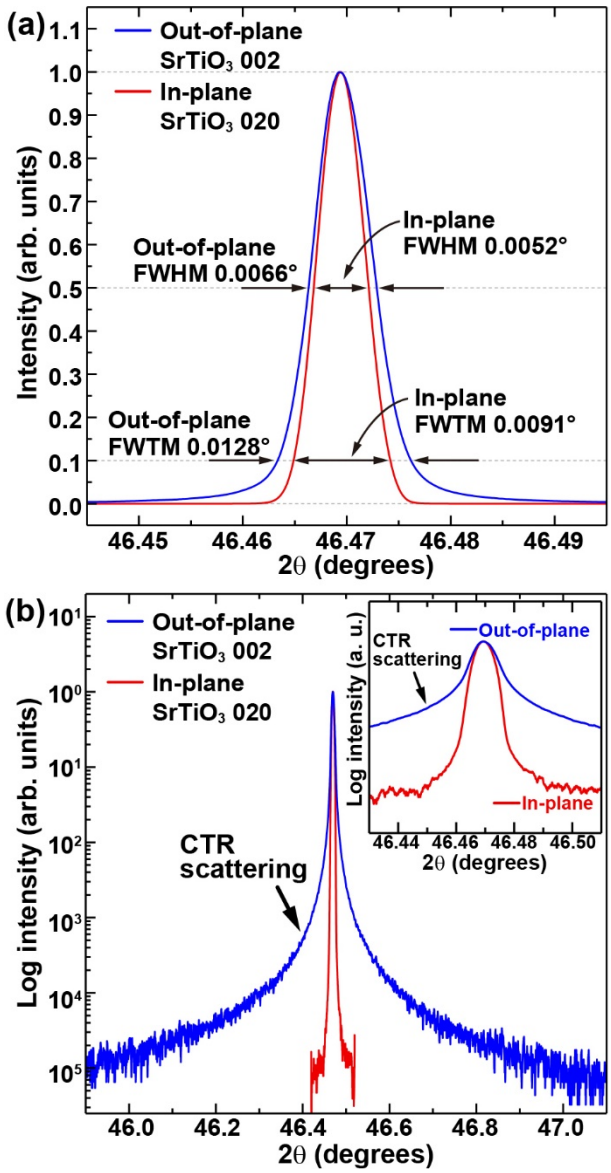

FIG. 1. (a) Linear and (b) log-scale intensities of out-of-plane and in-plane XRD patterns obtained for a pure $SrTiO_3$ single crystal. Reflections of the out-of-plane and in-plane XRD patterns are for 002 and 020 $SrTiO_3$, respectively. Rescaled data are shown in the inset at the upper right corner of (b).

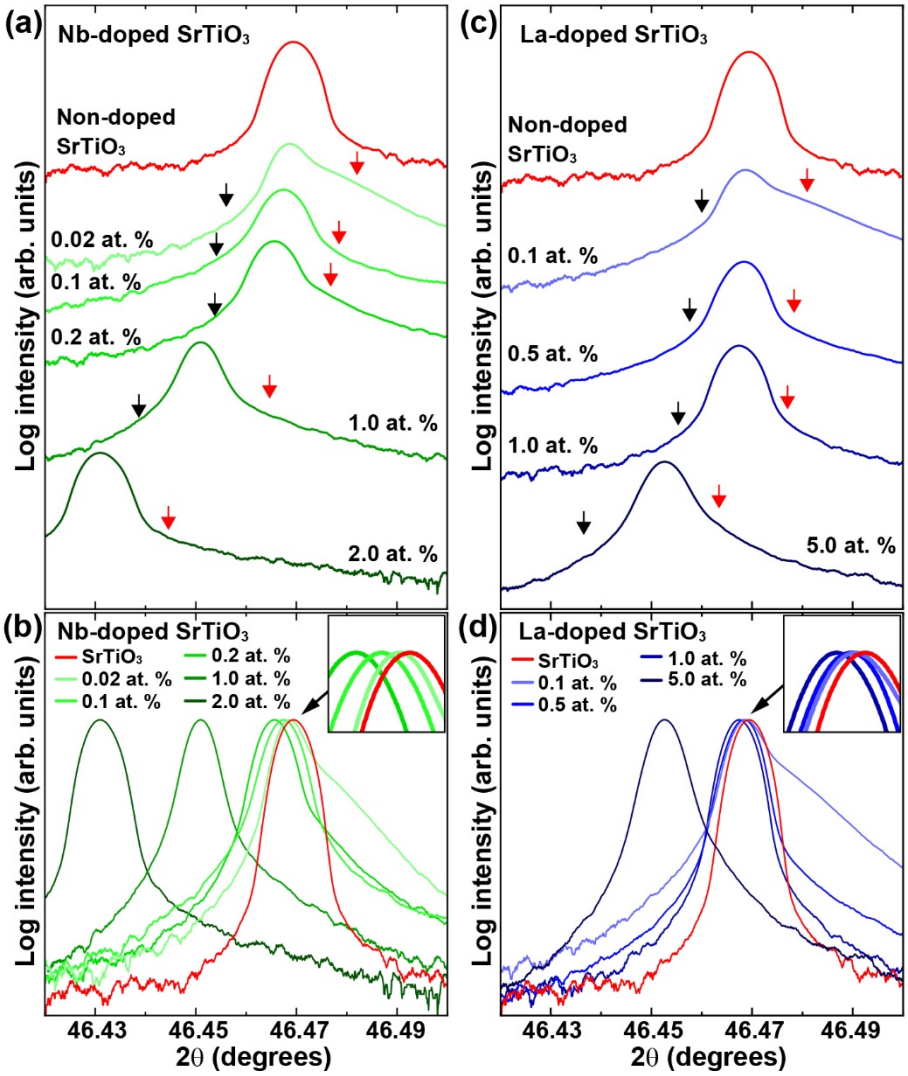

FIG. 2. In-plane XRD patterns obtained from 020 reflections of (a) Nb- and (b) La-doped $SrTiO_3$ single crystals. The red and black arrows in (a) and (b) indicate the intensities for the crystal lattice contraction and expansion, respectively. The rescaled data for Nb- and La-doped $SrTiO_3$ are shown in (c) and (d), respectively. The red-line XRD patterns in all the images are from the non-doped $SrTiO_3$ single crystal. The insets in the upper right corners of (c) and (d) show magnified images of the regions around the peaks of non-doped $SrTiO_3$.

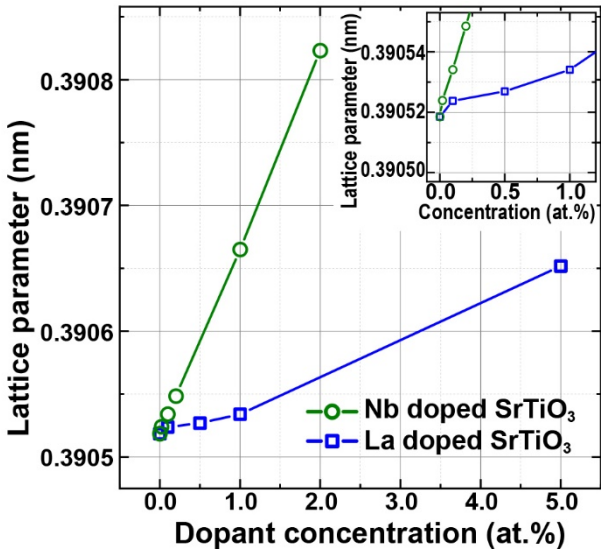

FIG. 3. Lattice parameters of Nb- and La-doped $SrTiO_3$ single crystals as a function of dopant concentration. The inset shows a magnified view of the low-concentration region.

Table 1. XRD measurements of non-, Nb-, and La-doped $SrTiO_3$ single crystals. Lattice parameters were calculated for a cubic perovskite structure, using Cu $K\alpha_1$ (λ = 0.154059 nm).

Sample	Concentration / at.%	020 Bragg peak 2θ / °	Lattice parameter / nm	020 Rocking curve FWHM / °
Non-doped $SrTiO_3$	-	46.46941	0.39051(9)	0.0030(0)
Nb-doped $SrTiO_3$	0.02	46.46873	0.39052(4)	0.0047(5)
	0.1	46.46745	0.39053(4)	0.0032(2)
	0.2	46.46563	0.39054(9)	0.0031(2)
	1	46.45095	0.39066(5)	0.0026(2)
	2	46.43107	0.39082(3)	0.0025(6)
La-doped $SrTiO_3$	0.1	46.46875	0.39052(4)	0.0049(6)
	0.5	46.46835	0.39052(7)	0.0030(2)
	1	46.46745	0.39053(4)	0.0039(0)
	5	46.45265	0.39065(2)	0.0041(2)

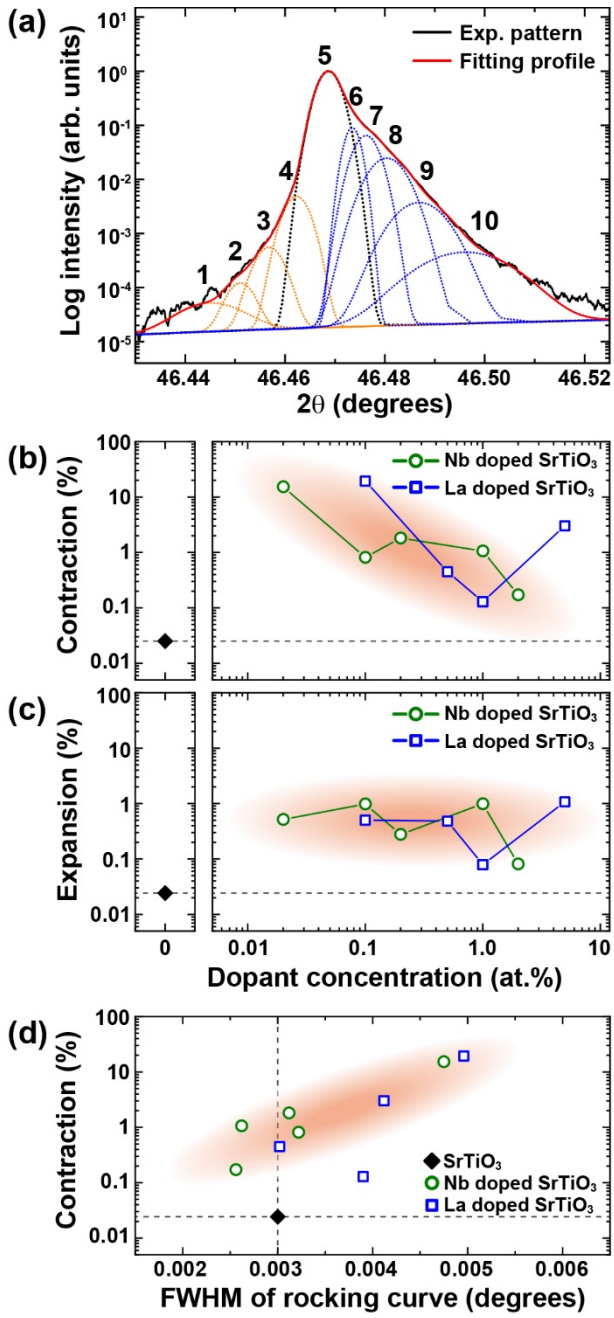

FIG. 4. (a) Fitting profile obtained using Gaussian functions for the experimental XRD pattern of 0.02 at.% Nb-doped $SrTiO_3$. The dotted black, orange, and blue lines indicate the Gaussian functions used for the main, expansion, and contraction intensities, respectively. Gaussian curves were numbered as labelled. (b) The contraction and (c) expansion intensity ratios calculated from the fitting results in Fig. S2, as a function of dopant concentration. Horizontal axes in (b) and (c), are log-scale, except for the values for non-doped $SrTiO_3$ shown as a black diamond on the left side of each graph. (d) Ratios of the contraction intensities as a function of the FWHM of the rocking curves. Gray dashed lines in (b), (c), and (d) are included to aid comparison between

Nb-doped, La-doped, and non-doped $SrTiO_3$.

Table 2. Lattice parameters estimated from the center of the Gaussian curves in Fig. 4. d_N is the lattice parameter estimated from the center of each Gaussian curve for a cubic perovskite structure. The last column lists differences between the lattice parameter corresponding to the 5th peak and that corresponding to the Nth peak.

Gaussian peak	Lattice parameter d_N / nm	d_N - d_5 / pm
1	0.39071(1)	0.19
2	0.39066(4)	0.14
3	0.39061(9)	0.09
4	0.39057(5)	0.05
5	0.39052(4)	0.00
6	0.39048(6)	-0.04
7	0.39046(5)	-0.06
8	0.39043(2)	-0.09
9	0.39038(0)	-0.14
10	0.39030(7)	-0.22

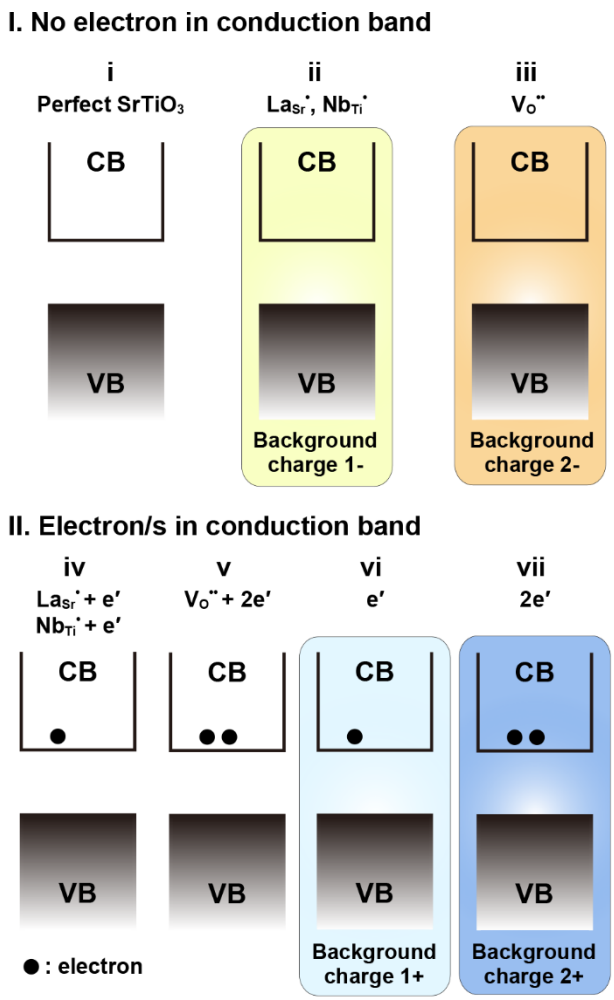

FIG. 5. Schematic diagram of electronic states in the valence band (VB) and conduction band (CB) of $SrTiO_3$, as used in the calculation models. There are no electrons in the CB for **i**: initial state, i.e., perfect $SrTiO_3$, **ii**: positively charged state 1+, i.e., $La_{Sr}^{\bullet}$ and $Nb_{Ti}^{\bullet}$, and iii: positively charged state 2+, i.e., $V_O^{\bullet\bullet}$. The total charges of supercells **ii** and **iii** were neutralized using jellium background charges of 1- and 2-, respectively. **iv**: neutral state with one electron in the CB, i.e., e′, $Nb_{Ti}^{\bullet}$+ e′, and $La_{Sr}^{\bullet}$+ e′; **v**: neutral state with two electrons in the CB, i.e.., $V_O^{\bullet\bullet}$; vi and vii: neutral states with one electron and two electrons, respectively, in the CB, i.e., e′ and 2e′. The total charge of the supercells of **vi** and **vii** was neutralized using jellium background charges of 1+ and 2+, respectively.

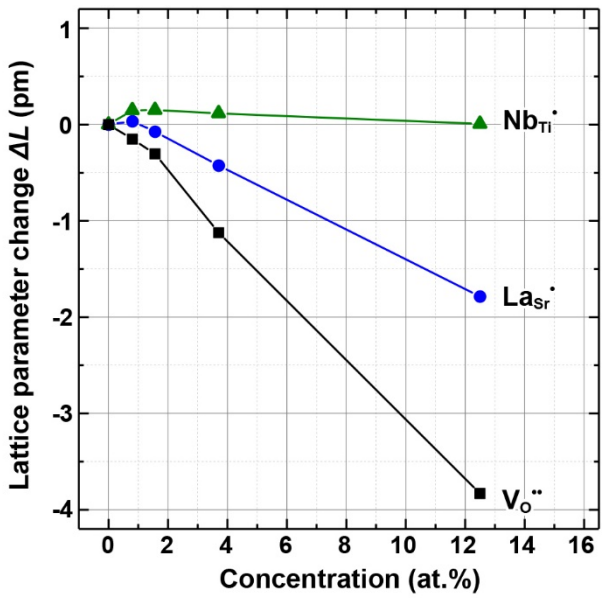

FIG. 6. Calculated lattice parameter changes as a function of dopant concentration for positively charged defects $Nb_{Ti}^{\bullet}$, $La_{Sr}^{\bullet}$, and $V_O^{\bullet\bullet}$ when there are no electrons in the CB of $SrTiO_3$.

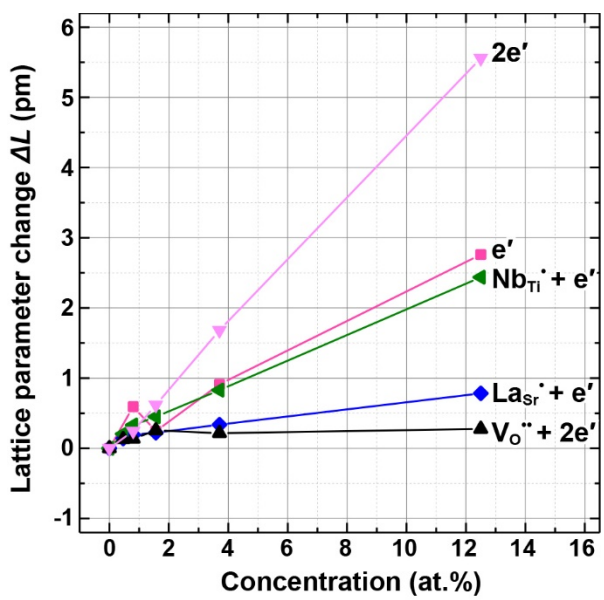

FIG. 7. Calculated lattice parameter changes as a function of dopant concentration for neutral defects $Nb_{Ti}^{\bullet}$+ e′, $La_{Sr}^{\bullet}$+ e′, $V_O^{\bullet\bullet}$ + 2e′, and free electrons e′, and 2e′ when electrons are present in the CB of $SrTiO_3$.

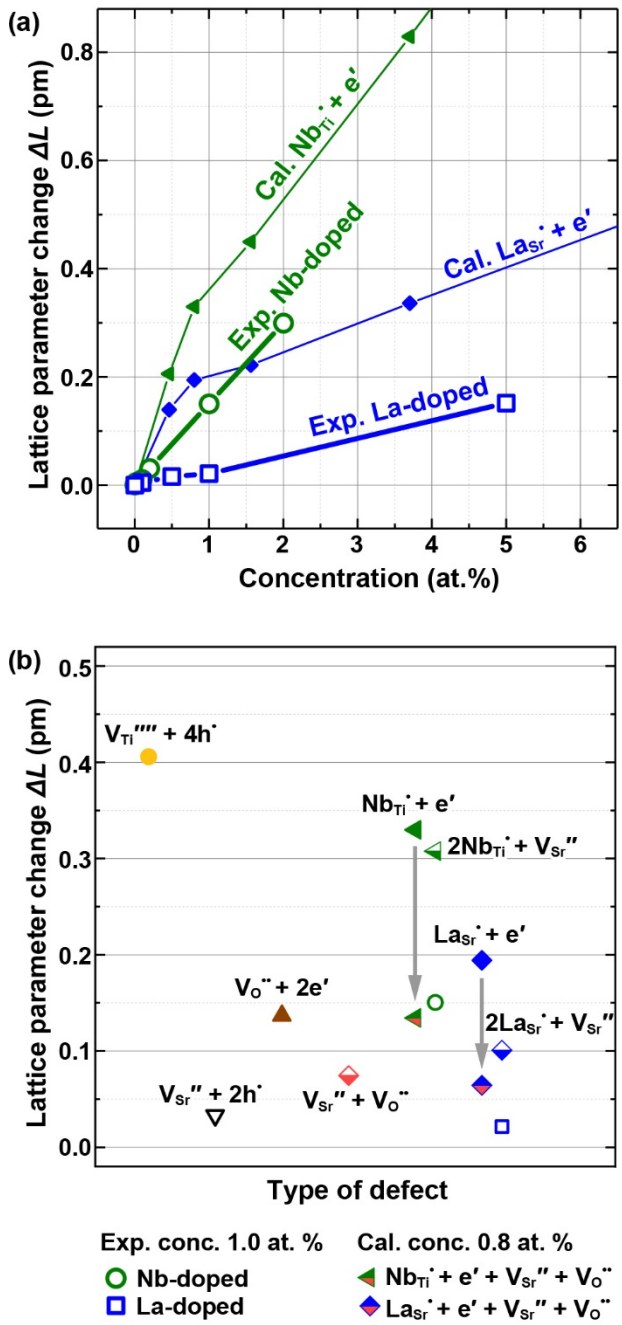

FIG. 8. Changes in (a) experimental (Exp.) and calculated (Cal.) lattice parameters of $SrTiO_3$ containing $Nb_{Ti}^{\bullet}$+ e′ and $La_{Sr}^{\bullet}$+ e′ defects, as a function of dopant concentration. (b) Changes in lattice parameters for V_{Ti}'' + $4h^{\bullet}$, V_{Sr}'' + $2h^{\bullet}$, $V_O^{\bullet\bullet}$ + 2e′, V_{Sr}'' + $V_O^{\bullet\bullet}$, $Nb_{Ti}^{\bullet}$+ e′, $La_{Sr}^{\bullet}$+ e′, $2Nb_{Ti}^{\bullet}$+ V_{Sr}'', and $2La_{Sr}^{\bullet}$+ V_{Sr}'' defect models, as well as each dopant with a V_{Sr}'' + $V_O^{\bullet\bullet}$ partial Schottky defect. Dopant and vacancy concentrations in the theoretical models were 0.8 at.% in all cases. The experimental results for 1.0 at.% Nb-doped (green circle) and La-doped (blue square) $SrTiO_3$ are included in (b) for comparison.

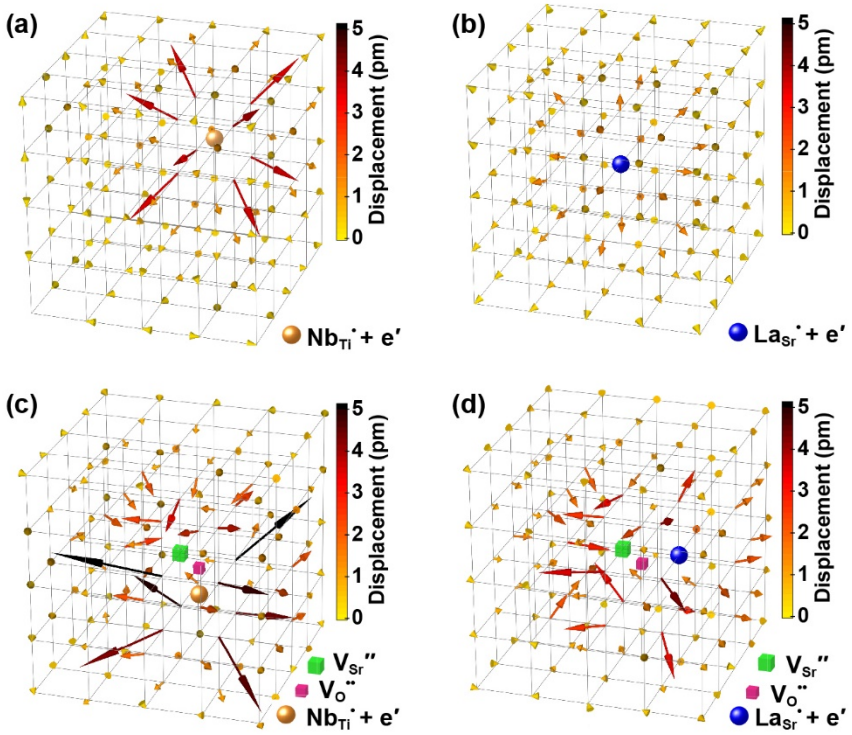

FIG. 9. Three-dimensional vector plots of Sr displacements around defects/dopants: (a) $Nb_{Ti}^{\bullet} + e'$, (b) $La_{Sr}^{\bullet} + e'$, (c) $Nb_{Ti}^{\bullet} + e' + V_{Sr}'' + V_O^{\bullet\bullet}$, and (d) $La_{Sr}^{\bullet} + e' + V_{Sr}'' + V_O^{\bullet\bullet}$. Sr, Ti, and O ions are located at the corners, centers, and face centers of the lattice cells, respectively. Vectors indicate the magnitudes and directions of Sr displacements from their ideal cubic perovskite lattice positions and are color-coded according to the scale bar on the right of each figure.

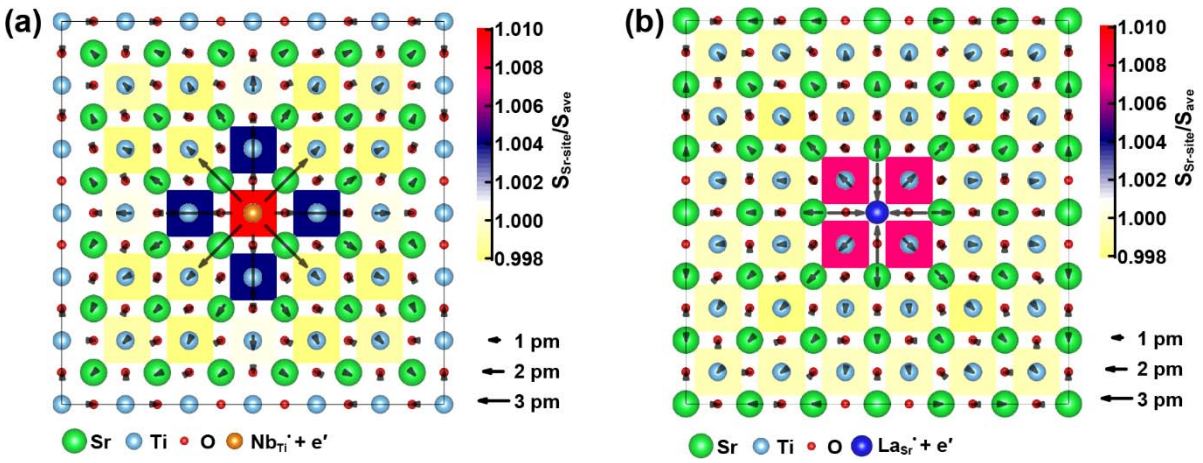

FIG. 10. Lattice models of (a) Nb- and (b) La-doped $SrTiO_3$ crystals as viewed along the <100> axis in the plane of the dopant atom. Background colors indicate the magnitude of $S_{Sr\text{-}site}/S_{ave}$ corresponding to the color scale on the right of each figure. The vector on each atom shows the direction and magnitude of displacement from its ideal lattice position. Vectors of O overlapping with those of Ti along the projected direction have been removed for clarity. Vectors at the bottom of (a) and (b) serve as a scale for the magnitude of displacement. Crystal structures were drawn using the VESTA program [59].

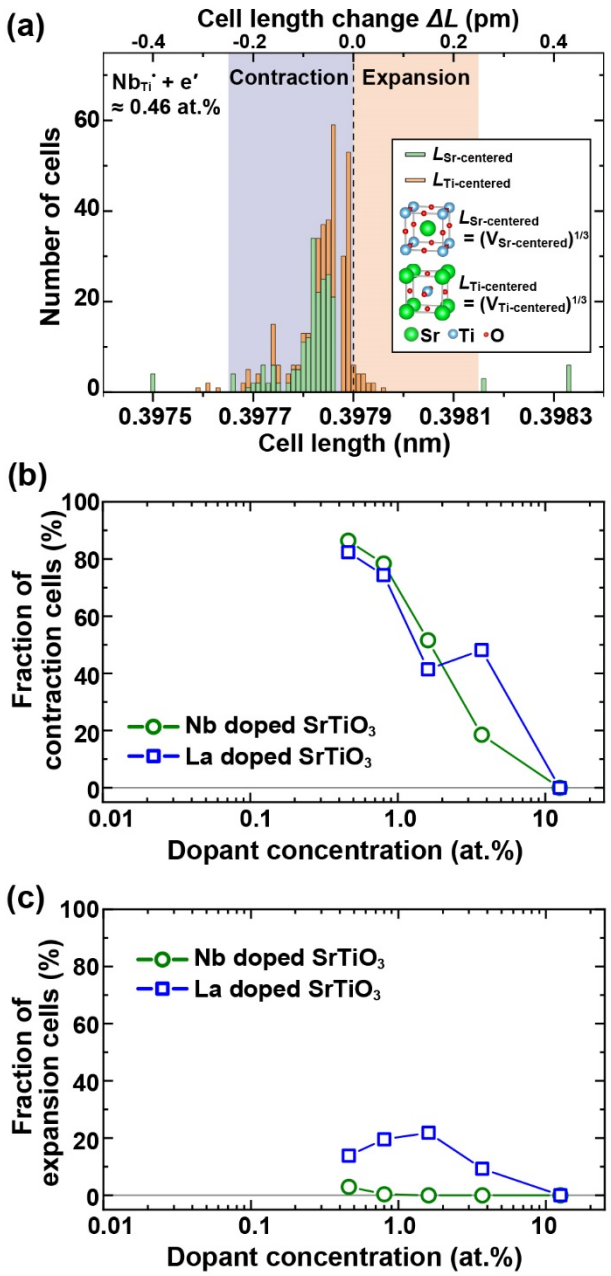

FIG. 11. (a) Histogram of cell lengths of Ti-centered and Sr-centered cells within relaxed supercells of Nb-doped $SrTiO_3$. For clarity, only a narrow range about the average lattice parameter (marked with a dotted line) is shown; results for the entire range are provided as Fig. S10a of Supplemental Material. (b), (c): Ratios of numbers of contracted and expanded cells, respectively, as a function of dopant concentration. The numbers of contracted and expanded cells were taken as those ±0.25 pm either side of the lattice parameter. As an aid to the eye,

lengths of contracted cells and expanded cells are highlighted with purple and orange backgrounds, respectively.

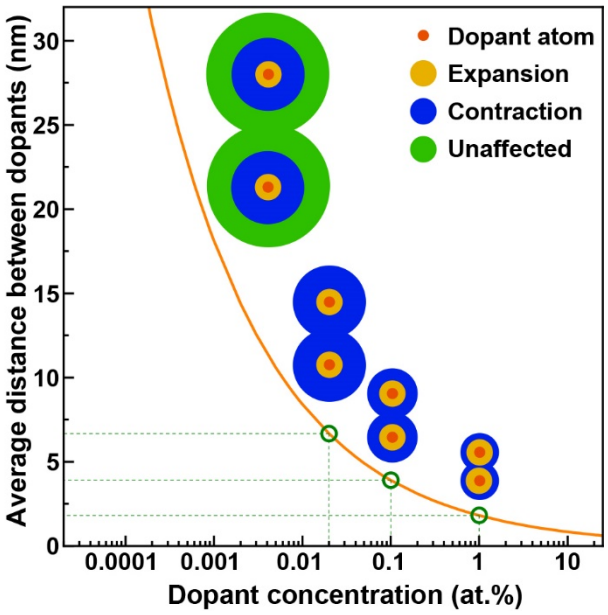

FIG. 12. Average distance between dopant atoms as a function of dopant concentration. Schematic models consisting of unaffected, expanded, and contracted regions around dopant atoms for each concentration are also shown.

References

[1] O. Tufte and P. Chapman, Phys. Rev. **155**, 796 (1967).

[2] J. Son, P. Moetakef, B. Jalan, O. Bierwagen, N. J. Wright, R. Engel-Herbert, and S. Stemmer, Nat. Mater. **9**, 482 (2010).

[3] S. Kobayashi, Y. Mizumukai, T. Ohnishi, N. Shibata, Y. Ikuhara, and T. Yamamoto, ACS Nano **9**, 10769 (2015).

[4] Y. Kozuka, M. Kim, C. Bell, B. G. Kim, Y. Hikita, and H. Y. Hwang, Nature **462**, 487 (2009).

[5] Y. Matsubara, K. S. Takahashi, M. S. Bahramy, Y. Kozuka, D. Maryenko, J. Falson, A. Tsukazaki, Y. Tokura, and M. Kawasaki, Nat. Commun. **7**, 11631 (2016).

[6] C. S. Koonce and M. L. Cohen, Phys. Rev. **163**, 380 (1967).

[7] H. Suzuki, H. Bando, Y. Ootuka, I. H. Inoue, T. Yamamoto, K. Takahashi, and Y. Nishihara, J. Phys. Soc. Jpn. **65**, 1529 (1996).

[8] S. Ohta, T. Nomura, H. Ohta, and K. Koumoto, J. Appl. Phys. **97**, 034106 (2005).

[9] H. Ohta *et al.*, Nat. Mater. **6**, 129 (2007).

[10] O. A. Marina, N. L. Canfield, and J. W. Stevenson, Solid State Ionics **149**, 21 (2002).

[11] H. Yamada and G. R. Miller, J. Solid State Chem. **6**, 169 (1973).

[12] P. Blennow, A. Hagen, K. Hansen, L. Wallenberg, and M. Mogensen, Solid State Ionics **179**, 2047 (2008).

[13] B. Zhang *et al.*, J. Mater. Chem. C **3**, 11406 (2015).

[14] A. Janotti, B. Jalan, S. Stemmer, and C. G. Van de Walle, Appl. Phys. Lett. **100**, 262104 (2012).

[15] S. A. Howard, J. K. Yau, and H. U. Anderson, J. Appl. Phys. **65**, 1492 (1989).

[16] I. Mahmud, M.-S. Yoon, I.-H. Kim, M.-K. Choi, and S.-C. Ur, J. Korean Phys. Soc. **68**, 35 (2016).

[17] R. D. Shannon, Acta Crystallogr. A **32**, 751 (1976).

[18] J. Liu, C. L. Wang, W. B. Su, H. C. Wang, P. Zheng, J. C. Li, J. L. Zhang, and L. M. Mei, Appl. Phys. Lett. **95**, 162110 (2009).

[19] P.-P. Shang, B.-P. Zhang, Y. Liu, J.-F. Li, and H.-M. Zhu, J. Electron. Mater. **40**, 926 (2010).

[20] Y. Tokuda, S. Kobayashi, T. Ohnishi, T. Mizoguchi, N. Shibata, Y. Ikuhara, and T. Yamamoto, Appl. Phys. Lett. **99**, 033110, 033110 (2011).

[21] S. Kobayashi, Y. Tokuda, T. Ohnishi, T. Mizoguchi, N. Shibata, Y. Sato, Y. Ikuhara, and T. Yamamoto, J. Mater. Sci. **46**, 4354 (2011).

[22] D. Freedman, D. Roundy, and T. Arias, Phys. Rev. B **80**, 0614108 (2009).

[23] T. Ohnishi, K. Shibuya, T. Yamamoto, and M. Lippmaa, J. Appl. Phys. **103**, 103703 (2008).

[24] S. Kobayashi, Y. Ikuhara, and T. Yamamoto, Appl. Phys. Lett. **102**, 231911 (2013).

[25] S. T. Pantelides, Rev. Mod. Phys. **50**, 797 (1978).

[26] W. Wunderlich, H. Ohta, and K. Koumoto, Phys. B Condens. Matter. **404**, 2202 (2009).

[27] J. D. Baniecki, M. Ishii, H. Aso, K. Kurihara, and D. Ricinschi, J. Appl. Phys. **113**, 013701 (2013).

[28] A. Janotti, D. Steiauf, and C. G. Van de Walle, Phys. Rev. B **84**, 201304 (2011).

[29] Y. J. Chang, G. Khalsa, L. Moreschini, A. L. Walter, A. Bostwick, K. Horn, A. H. MacDonald, and E. Rotenberg, Phys. Rev. B **87**, 115212 (2013).

[30] R. Berger, C. Fennie, and J. Neaton, Phys. Rev. Lett. **107**, 146804 (2011).

[31] B. Himmetoglu, A. Janotti, H. Peelaers, A. Alkauskas, and C. G. Van de Walle, Phys. Rev. B **90**, 241204 (2014).

[32] H. Frederikse and W. Hosler, Phys. Rev. **161**, 822 (1967).

[33] K. Omote, J. Phys.: Condens. Matter. **22**, 474004 (2010).

[34] B. L. Henke, E. M. Gullikson, and J. C. Davis, At. Data Nucl. Data Tables **54**, 181 (1993).

[35] X-Ray attenuation length [http://henke.lbl.gov/optical_constants/atten2.html].

[36] Z. Salman *et al.*, Phys. Rev. B **83**, 224112 (2011).

[37] M. Schmidbauer, A. Kwasniewski, and J. Schwarzkopf, Acta Crystallogr. B **68**, 8 (2012).

[38] D. Cuong, B. Lee, K. Choi, H.-S. Ahn, S. Han, and J. Lee, Phys. Rev. Lett. **98**, 115503 (2007).

[39] N. Orita, Jpn. J. Appl. Phys. **49**, 055801 (2010).

[40] S. Okamoto, A. J. Millis, and N. A. Spaldin, Phys. Rev. Lett. **97**, 056802 (2006).

[41] G. Kresse and J. Furthmüller, Phys. Rev. B **54**, 11169 (1996).

[42] G. Kresse and D. Joubert, Phys. Rev. B **59**, 1758 (1999).

[43] K. Page, T. Kolodiazhnyi, T. Proffen, A. K. Cheetham, and R. Seshadri, Phys. Rev. Lett. **101**, 205502 (2008).

[44] S. R. Andrews and R. A. Cowley, J. Phys. C-Solid State Phys. **18**, 6427 (1985).

[45] I. K. Robinson, Phys. Rev. B **33**, 3830 (1986).

[46] K. Nassau and A. E. Miller, J. Cryst. Growth **91**, 373 (1988).

[47] T. Tanaka, K. Matsunaga, Y. Ikuhara, and T. Yamamoto, Phys. Rev. B **68**, 205213 (2003).

[48] R. Moos and K. H. Hardtl, J. Am. Ceram. Soc. **80**, 2549 (1997).

[49] F. A. Kröger and H. J. Vink, Solid State Phys. **3**, 307 (1956).

[50] Y. Kozuka, Y. Hikita, C. Bell, and H. Y. Hwang, Appl. Phys. Lett. **97**, 012107 (2010).

[51] A. E. Paladino, J. Am. Ceram. Soc. **48**, 476 (1965).

[52] H. J. Scheel, J. G. Bednorz, and P. Dill, Ferroelectrics **13**, 507 (1976).

[53] Y. Jun-ichi, S. Takeshi, and Y. Junji, Jap. J. Appl. Phys. **40**, 6536 (2001).

[54] C. Rodenbucher, M. Luysberg, A. Schwedt, V. Havel, F. Gunkel, J. Mayer, and R. Waser, Sci. Rep. **6**, 32250 (2016).

[55] P. I. Nabokin, D. Souptel, and A. M. Balbashov, J. Cryst. Growth **250**, 397 (2003).

[56] P. Gay, P. B. Hirsch, and A. Kelly, Acta Metall. **1**, 315 (1953).

[57] J. E. Ayers, J. Cryst. Growth **135**, 71 (1994).

[58] Y. Kim, A. S. Disa, T. E. Babakol, and J. D. Brock, Appl. Phys. Lett. **96**, 251901 (2010).

[59] K. Momma and F. Izumi, J. Appl. Crystallogr. **41**, 653 (2008).

665